

12 Microstructures in Rough Metal Surfaces: Electromagnetic Mechanism in Surface-Enhanced Raman Spectroscopy

J. A. Sánchez-Gil¹, J. V. García-Ramos¹, and E. R. Méndez²

¹ Instituto de Estructura de la Materia, Consejo Superior de Investigaciones Científicas, Serrano 121, E-28006 Madrid, Spain,

² Division de Física Aplicada, Centro de Investigación Científica y de Educación Superior de Ensenada, Ensenada, Baja California 22800 Mexico

Abstract. One of the two fundamental mechanisms underlying Surface-Enhanced Raman Scattering (SERS) is the existence of large electromagnetic (EM) fields in the vicinity of the rough metal substrates that are used as substrates. Surface roughness below the micron scale plays a relevant role in this process, due to the roughness-induced excitation of surface-plasmon polaritons. Since in many scattering configurations dipolar and/or electrostatic approximations cannot be employed, we study this EM mechanism from the rigorous standpoint of classical Maxwell equations. By means of numerical simulation calculations based on the Green's theorem integral equation formulation, the linearly polarized electromagnetic field scattered from one-dimensional, randomly rough metal surfaces is obtained. In particular, Ag, Au, and Cu surfaces are considered possessing fractal properties analogous to those observed in colloidal aggregates or coldly deposited films commonly used in SERS experiments. We analyze the influence of the roughness parameters on the near field intensity. The enhancement factor of the SERS signal is assumed to be proportional to the square of that of the near field intensity at the pump frequency; in light of the random nature of the roughness, the analysis is performed on the probability density function of the enhancement factor. The optimum pump frequency is obtained from the spectral dependence of both the average field enhancement and the absorption. In addition to the near field intensity calculations, the far field scattered from such random self-affine fractals is studied, revealing interesting features in the angular distribution, such as incoherent peaks at the specular direction, and weak backscattering peaks for the rougher surfaces that also yield large near field enhancements.

1 Introduction

Raman spectroscopy is a very useful technique to study the structure of all kind of materials. However, the weakness of the Raman signal is a drawback that forces the experimentalist to use high-power light and extremely sensitive detectors. During the 60's, the discovery of lasing gave an enormous impulse to the technique owing to the dramatic increase in the radiation intensity on the sample. Later on, in the mid 70's, Raman spectroscopy underwent a second revolution with the observation of Surface-Enhanced Raman Scattering (SERS) coming from a molecule adsorbed onto a rough surface (see Fig. 1).

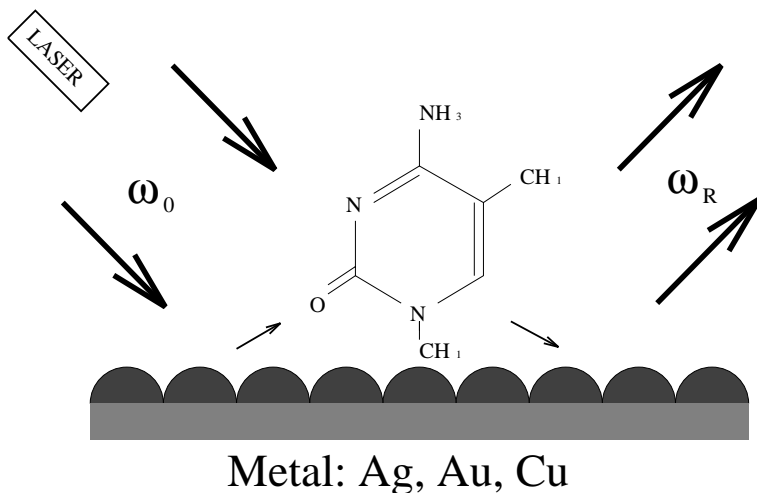


Fig. 1. Illustration of surface-enhanced Raman scattering.

SERS was first observed by Fleischmann et al. [1] for pyridine adsorbed at silver electrodes. Then Jeanmaire and R. P. Van Duyne [2] and Albrecht and Creighton [3] independently suggested that this high increase in the inelastic Raman signal is produced by the intensification of the electromagnetic (EM) field near the metal surface of the electrode where the pyridine is adsorbed. Typically, SERS enhancements factors with respect to conventional Raman of six orders of magnitude were accounted for. Thus far the origin of the SERS phenomenon is not entirely clear, but it is generally accepted that an EM enhancement mechanism is to a large extent responsible for it [4]–[8]. (In addition to the EM mechanism, other effects, such as resonance Raman scattering [9] or chemisorption [10], can have a multiplicative impact upon the SERS signal.)

The amount of theoretical work dedicated to the EM mechanism in SERS is enormous. It is out of the scope of this chapter to review all the existing theories and models; for that purpose, there are various excellent review articles [4]–[8], [11] in the literature, which refer to SERS theories in certain depth. It is interesting to note, however, that most of the numerous theoretical works devoted to the description of the EM mechanism rely on the electrostatic and/or dipolar approximations, and use as surface models extremely simple geometries. The common qualitative picture to all those models is the fact that the EM field enhancement (FE) stems from the roughness-induced excitation of surface-plasmon polaritons [12] (SPP) by the incoming light, resulting in large EM fields in the vicinity of the metal surface that strongly polarize the adsorbed molecules. A similar EM enhancement is assumed to occur at the Raman-shifted frequencies, which combined with the former direct enhancement may give rise to an overall FE factor on the order of or above 10^4 . A SPP can be either propagating along a continuous

surface (extended SPP), confined within metal particles (particle plasmon resonances), or even localized due to Anderson localization (localized SPP); of course, some of these effects may take place altogether on real SERS metal substrates.

Moreover, from all of these studies and abundant experimental evidence, it has been commonly accepted that a *rough surface* on which the adsorbate is located (within a few angstroms) is crucial to observe SERS. Several kinds of rough metal surfaces have been employed as SERS substrates: electrodes, films, and colloids. All of them exhibit microstructures, being even necessary the presence of corrugation of scale of the order of or below a tenth of a micron. Cold deposited silver islands films and silver or gold colloids are the most widely used. In the case of colloids, their aggregation is necessary to obtain SERS effect [13]-[16]. Interestingly enough, the internal structure of these films and aggregates can be in most cases characterized in terms of fractal properties: self-affinity in the case of films [17] and self-similarity in the case of aggregates [14,15]. In general, many aggregation and surface growth processes create such structures [18,19].

Therefore, inasmuch as the quantitative evaluation of the surface EM field is central to the SERS effect, a rigorous knowledge of the EM scattering process for surface models as realistic as possible is evidently needed. In recent years, the theoretical efforts have been directed towards either describing approximately realistic surface models [14], [20]-[22], or using the full EM theory to study simplistic surface models (though introducing increasingly complex properties) [23]; in addition to that, some efforts have been made to combine both the rigorous EM theory with complex, realistic surface models [24]-[26].

In what follows, we will review the latter works, which address the issue of the direct EM enhancement on continuous, fractal metal surfaces from the rigorous standpoint of classical electrodynamics. To that end, we present in Sect. 2 the exact integral equations formulation of the EM wave scattering, not restricted to the limitations of electrostatic and/or dipolar approximations. This formulation has been successfully employed through numerical simulation calculations to study the far field scattered from one-dimensional, randomly rough, either metal or dielectric, surfaces [27]-[29]. In Sect. 4, we will apply it to calculate the linearly-polarized EM field in the vicinity of self-affine fractal surfaces (described in Sect. 3) of Ag, Au, and Cu, similar to those mentioned above that are used as SERS substrates (cf. [24,26]). Section 5 analyzes in detail the occurrence of FE and the dependence on both roughness parameters (fractal dimension and rms height deviation) and excitation wavelength (cf. [24,26]). The angular distribution of the far field intensity scattered from such metal surfaces (cf. [25]) is studied in Sect. 6. Finally, the main advances of all these works are summarized in Sect. 7, and some guidelines on ongoing work and foreseen perspectives included in Sect. 8.

2 EM Scattering Theory

Let us model the geometry associated with typical SERS experimental configurations exploiting metal surfaces by means of a one-dimensionally rough, vacuum-metal interface $z = \zeta(x)$. The metal occupying the lower half-space [$z \leq \zeta(x)$] is characterized by an isotropic, homogeneous, frequency-dependent dielectric function $\epsilon^<(\omega)$. This surface is illuminated by a monochromatic, linearly polarized Gaussian beam of frequency $\omega = 2\pi/\lambda$ and half-width W incident at an angle θ_0 measured counterclockwise with respect to the positive z axis.

The restrictions to one-dimensional surfaces and linearly polarized incident beams have the advantage that notably simplify the formulation, while still rigorously considering the scattering processes relevant to interpret the SERS EM mechanism. In fact, under such conditions, we can reduce the initial three-dimensional vectorial problem to a two-dimensional scalar one, where the EM field is entirely described by the y -component [denoted by $U_\beta(\mathbf{r}, \omega)$, with $\mathbf{r} \equiv (x, z)$] of, respectively, the electric field for $\beta = s$ polarization (transversal electric) and the magnetic field for $\beta = p$ polarization (transversal magnetic). It should be emphasized that this simplification, unlike the case of straight scalar formulations, stems only from the scattering geometry, so that the full vector, EM character of the problem is preserved.

Our rigorous calculation method is based upon the exact integral equations formulation of the above mentioned scattering problem [26]-[29]. This formulation can be briefly summarized as follows. On the basis of the Helmholtz equations satisfied by the field in the upper $U_\beta^>(\mathbf{r}, \omega)$ ($z > \zeta$) and lower $U_\beta^<(\mathbf{r}, \omega)$ ($z < \zeta$) semi-infinite half-spaces, and by applying the Green's theorem and recalling the radiation conditions at infinity, we are led to the following four integral equations:

$$U_\beta^{(i)}(\mathbf{r}, \omega) + \frac{1}{4\pi} \int_{-\infty}^{\infty} dx' \left[U_\beta^>(\mathbf{r}', \omega) \frac{\partial G^>(\mathbf{r}, \mathbf{r}' : \omega)}{\partial n'} - G^>(\mathbf{r}, \mathbf{r}' : \omega) \frac{\partial U_\beta^>(\mathbf{r}', \omega)}{\partial n'} \right] : \gamma' = U_\beta^>(\mathbf{r}, \omega), \quad z > \zeta(x) \quad (1)$$

$$= 0, \quad z < \zeta(x); \quad (2)$$

$$- \frac{1}{4\pi} \int_{-\infty}^{\infty} dx' : \left[U_\beta^<(\mathbf{r}', \omega) \frac{\partial G^<(\mathbf{r}, \mathbf{r}' : \omega)}{\partial n'} - G^<(\mathbf{r}, \mathbf{r}' : \omega) \frac{\partial U_\beta^<(\mathbf{r}', \omega)}{\partial n'} \right] \gamma' = 0, \quad z > \zeta(x) \quad (3)$$

$$= U_\beta^<(\mathbf{r}, \omega), \quad z < \zeta(x); \quad (4)$$

where $\mathbf{r}' = (x', z' = \zeta(x'))$ and the normal derivative is $\partial/\partial n \equiv (\hat{\mathbf{n}} \cdot \nabla)$ [with $\hat{\mathbf{n}} \equiv \gamma^{-1}(-\zeta'(x), 0, 1)$ and $\gamma = (1 + (\zeta'(x))^2)^{1/2}$]. The Green's function G is

given by the zeroth-order Hankel function of the first kind. In our work, the incident field, as mentioned above, is given by the Gaussian beam [27]:

$$U_{\beta}^{(i)}((x, z), \omega) = \exp \left[i \frac{\omega}{c} (x \sin \theta_0 - z \cos \theta_0) (1 + w(x, z)) \right] \times \exp \left[-W^{-2} (x \cos \theta_0 + z \sin \theta_0)^2 \right], \quad (5)$$

$$w(x, z) = \frac{c^2}{\omega^2 W^2} \left[2W^{-2} (x \cos \theta_0 + z \sin \theta_0)^2 - 1 \right]. \quad (6)$$

The integral equations (4) enable us to obtain an exact solution for the scattering of a *s*- or *p*-polarized electromagnetic wave. A set of two coupled integral equations can be obtained by using (1) and (3) as extended boundary conditions with the aid of the continuity conditions across the interface:

$$U_{\beta}^{>}(\mathbf{r}, \omega) |_{z=\zeta^{(+)}(x)} = U_{\beta}^{<}(\mathbf{r}, \omega) |_{z=\zeta^{(-)}(x)}, \quad (7)$$

$$\left[\frac{\partial U_{\beta}^{>}(\mathbf{r}, \omega)}{\partial n} \right]_{z=\zeta^{(+)}(x)} = \frac{1}{\alpha_{\beta}} \left[\frac{\partial U_{\beta}^{<}(\mathbf{r}, \omega)}{\partial n} \right]_{z=\zeta^{(-)}(x)}, \quad (8)$$

with $\alpha_s = 1$ and $\alpha_p = \epsilon^{<}/\epsilon^{>}$, and $\zeta^{(\pm)}(x) = \lim_{\varepsilon \rightarrow 0} (\zeta(x) \pm \varepsilon)$. As shown in detail in [28], upon numerically solving the resulting system of integral equations for the surface field and its normal derivative, which play the role of source functions, the scattered field in the entire space can be calculated from (1) and (2). Therefore, for our purpose, the exact, self-consistent surface field results directly from one of the source functions, and then (1) will be used to calculate such total field at any other position \mathbf{r} in vacuum $z > \zeta$. Note that this total field consists of the incident field plus the scattered field, the latter being in turn given by the surface integral in the left-hand side of (1). We will deal in the numerical calculations with the former surface integral as shown in (1), and also with its far field expression, which yields the angular distribution of scattered light (θ_s being the scattering angle measured clockwise with respect to the positive z axis):

$$I_{\beta}(\theta_s) = \frac{\omega^2}{2(2\pi)^{3/2} c^2 W} [1 - c^2 (1 + 2 \tan^2 \theta_0) / 2\omega^2 W^2]^{-1} \times \left| \int_{-\infty}^{\infty} dx : \exp [-i(\omega/c)(x \sin \theta_s + \zeta(x) \cos \theta_s)] \times \left\{ [\cos \theta_s - \zeta'(x) \sin \theta_s] U_{\beta}^{>}(x, \zeta(x), \omega) - i(c/\omega) \gamma \frac{\partial U_{\beta}^{>}(x, z, \omega)}{\partial n} \right\} \right|_{z=\zeta^{(+)}(x)}^2. \quad (9)$$

With regard to the near EM field, apart from the resulting total field intensity

$$I_{\beta}(\mathbf{r}, \omega) = |U_{\beta}^{>}(\mathbf{r}, \omega)|^2,$$

we define the EM field enhancement factor as the normalized intensity:

$$\sigma_{\beta}(\omega) = \frac{I_{\beta}(\omega)}{|U_{\beta}^{(i)}(\omega)|^2}. \quad (10)$$

(Strictly speaking, σ_{β} makes full sense for \mathbf{r} in the region illuminated by the central spot of the incident beam.) Relevant to the SERS signal is the product of FE at the excitation and Raman frequencies (respectively, ω and ω') which can be approximated by the square of the FE at the pump frequency [23,26].

The numerical implementation of the above given formulation relies on the conversion of the integral equations into linear equations: By means of a quadrature scheme the surface is truncated to a length L consisting of N sampling points [28]. In practice, for every realization of the random surface, it reduces to solving a system of $2N$ complex linear equations for the source functions, followed by a vector-matrix multiplication to obtain the scattered field at each position in the vacuum half-space. Furthermore, when statistical quantities such as ensemble averages ($\langle \dots \rangle$) or probability density functions (PDF) are needed, the procedure is repeated for a sufficiently large number N_r of surface profile realizations (ergodicity is assumed). Finally, various numerical tests are performed as regards energy conservation, reciprocity, and convergence with increasing N and N_r (cf. [28]).

It should be mentioned that the assumption that the upper propagating medium ($z > \zeta(x)$) is vacuum with $\epsilon^> = 1$ can be easily modified to account for any other isotropic and homogeneous dielectric medium by conveniently renormalizing the dielectric functions and the incoming beam wavelength [30]. Also, despite the fact that the region occupied by the metal is semi-infinite, our theoretical model can be in practice applied to metal films on a semi-infinite substrate provided that their thickness be sufficiently large compared to the metal skin depth $d = c(\epsilon^>(\omega))^{-1/2}/\omega$. However, in the case of Ag island films for which plasmon resonances on isolated particles are crucial [5,6], the surface geometry should be correspondingly modified to account for such close contours (see e.g. Madrazo et al. in this book).

3 Fractal Surface Model

The theoretical formulation described in the preceding section can be applied to any kind of either random or deterministic surfaces provided that the profile function is known. We restrict to random fractal surfaces that reproduce the properties of many naturally occurring surfaces [17,19,31]. These are self-affine fractals, which are modeled henceforth by the time dependence of the trace [i.e. the x dependence of the height $z = \zeta(x)$] of a one-dimensional fractional Brownian motion (fBm). Self-affinity implies that the scaling relations possess different ratios depending on the direction (along x and z). It is characterized by the local fractal dimension $D = 2 - H$, H being the Hurst

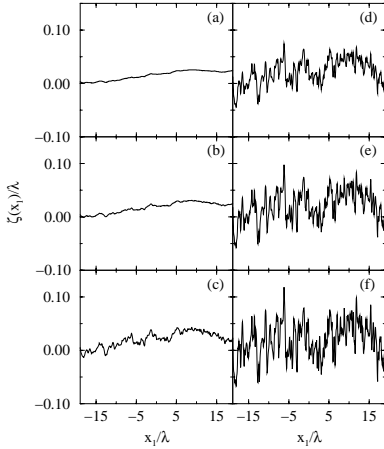


Fig. 2. Realizations of the self-affine random fractal profiles numerically generated by means of the Voss' algorithm: $\delta/\lambda = 0.05$. The corresponding fractal dimensions are: (a) $D = 1$; (b) $D = 1.2$; (c) $D = 1.5$; (d) $D = 1.8$ (e) $D = 1.9$; and (f) $D = 1.99$.

exponent; the global fractal dimension is 1 (recall that for self-affine fractals the fractal dimension is not uniquely defined). In order to generate such fractal surfaces to an arbitrary resolution, we employ the successive random addition algorithm proposed by Voss [31].

By assigning a length $L = 52.7\mu\text{m}$ to each realization, the sequences of random fractal numbers numerically generated as mentioned above are mapped onto real surfaces of the kind employed in SERS experiments [16,17]. The resolution ($N_f = 1024$) is such that the minimum size of the surface asperities $\Delta x = 51.45\text{ nm}$ closely resembles the typical sizes of the metal particles that form some widely used SERS substrates [13,16]. Moreover, to reproduce such slowly varying profile below the lower spatial limit associated with the particle shape, a cubic spline interpolation with $n_i = 1$ points is performed. In this regard, it should be remarked that the rms heights $[\delta = \langle \zeta^2(x) \rangle^{1/2}]$ of the fractal surfaces studied throughout this work are also comparable with such typical sizes (see Fig. 2).

4 Near EM Field

We now present the numerical results obtained as described in Sect. 3 for the self-affine random fractal surfaces defined in Sect. 2. In all the cases shown below, unless otherwise stated, a length $L = 20.58\mu\text{m}$ consisting of $N = 800 = 400(n_i + 1)$ (extracted from $N_f = 1024$) is taken per realization, and the intercept of the Gaussian incident beam with the plane of the mean surface is kept constant regardless of the angle of incidence ($W/\cos\theta_0 = L/4$). This intercept illuminates a sufficiently large region of the fractal surface in terms of the range of incident wavelengths considered below ($0.4\mu\text{m} < \lambda < 1.1\mu\text{m}$). It should be emphasized that the choice of scattering parameters, leaving aside its being very realistic from the experimental standpoint, guarantees

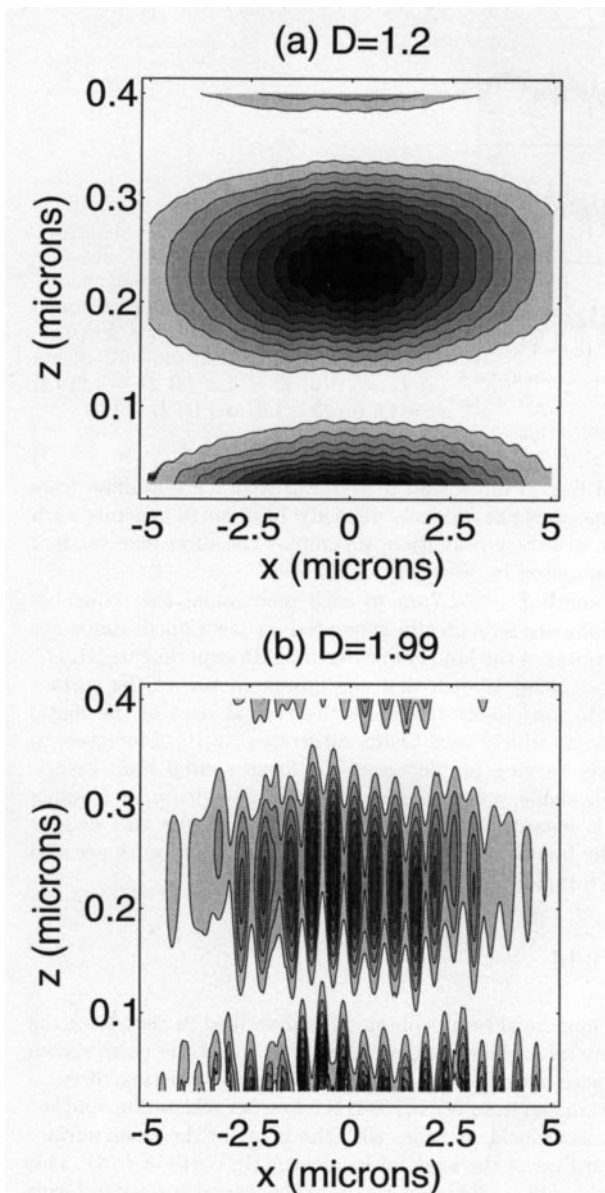


Fig. 3. Contour density plot of the near field intensity resulting from the p -polarized scattering from a Ag fractal surface with $\theta_0 = 0^\circ$, $\delta = 25.725$ nm, $\lambda = 514.5$ nm ($\epsilon^< = -9.4 + i0.8$), $L = 10.29$ μm , $W = L/4 \cos \theta_0$, and $N = 400$. (a) $D = 1.2$, and the maximum intensity is $I_{\max} = 0.05$; (b) $D = 1.99$ and $I_{\max} = 0.11$.

additionally that the random surface exhibits self-affine scaling for a large range of lengths (approximately from below one tenth of the wavelength to beyond the illuminated area), thus covering the relevant scaling interval of this scattering problem.

In Fig. 3, the intensity of the p -polarized EM near field for normal incidence is shown in a region of about one wavelength above two Ag fractal surfaces of length $L = 10.29 \mu\text{m}$ $\delta = 25.7 \text{ nm}$, corresponding, respectively, to $D = 1.2$ (Fig. 3(a)) and $D = 1.99$ (Fig. 3(b)). At the wavelength of the incident beam ($\lambda = 514.5 \text{ nm}$), the dielectric function of silver is [32] $\epsilon_{Ag}^<(\omega) = -9.4 + i0.8$. Both in Figs. 3(a) and (b), it is evident that the incident Gaussian beam impinging on the Ag surface (lower part of the plot) is scattered due to the surface roughness: The interference between the incident and scattered fields gives rise to the observed intensity pattern with horizontal fringes of length limited by the beam width. In Fig. 3(a) the EM field appears to be weakly scattered, and a strong specularly reflected beam results in a well defined interference pattern, with the first maximum above the surface close to $z = c(2\pi - \phi_R)/(2\omega) = 231 \text{ nm}$ (ϕ_R being the phase shift introduced by the Fresnel coefficient on reflection). The more rugged surface profile with $D = 1.99$ used in obtaining the results shown in Fig. 3(b) scatters the EM field more strongly, thus leading to both a weaker and more distorted reflected beam (the interference pattern appears blurred), and to larger EM field intensities in the proximity of the surface $z < \lambda/4 = 128.625 \text{ nm}$.

To gain physical insight into the origin of such FE, let us calculate the EM field resulting from subtracting the incident and the singly scattered (in the Geometrical Optics sense) fields from the total field. The latter field is numerically obtained from the surface integral in the lhs of (1), upon replacing the exact source functions by their Kirchhoff approximation expressions [24,26]:

$$U_\beta([x, \zeta(x)], \omega) = [1 \mp R_\beta(\theta(x))] U_\beta^{(i)}([x, \zeta(x)], \omega), \quad (11)$$

R_β being the Fresnel coefficient for the local angle of incidence $\theta(x) = \theta_0 - d\zeta/dx$, and the minus (respectively, plus) sign corresponding to $\beta = s$ (respectively, $\beta = p$); a similar expression holds for the normal derivative [28]. In Fig. 4, the intensity of the component of the doubly (and highly) scattered EM fields is shown for the same fractal surfaces as used in Fig. 3, but for a smaller region in the vacuum up to $z \approx \lambda/4$ above the surface. We observe in both Figs. 4(a) and 4(b) an interference pattern whose spatial frequency along the surface indicates the existence of SPP with wave vector $k = (\omega/c)(\epsilon^<(\omega)/(1 + \epsilon^<(\omega)))^{1/2}$ propagating in opposite directions. Moreover, the excitation of SPP has been verified by calculating the intensity from Fig. 4(b) along the line $x = 0$ away from the interface, confirming that it closely follows the well known SPP exponential decay in the form $\exp[-2\beta(\omega)z]$ with decay length $\ell = (2\beta(\omega))^{-1} = \Re[c(-1 - \epsilon_{Ag}^<(\omega))^{1/2}/(2\omega)] \approx 119 \text{ nm}$ (\Re denoting the real part). Whereas for the surface with lower fractal dimension

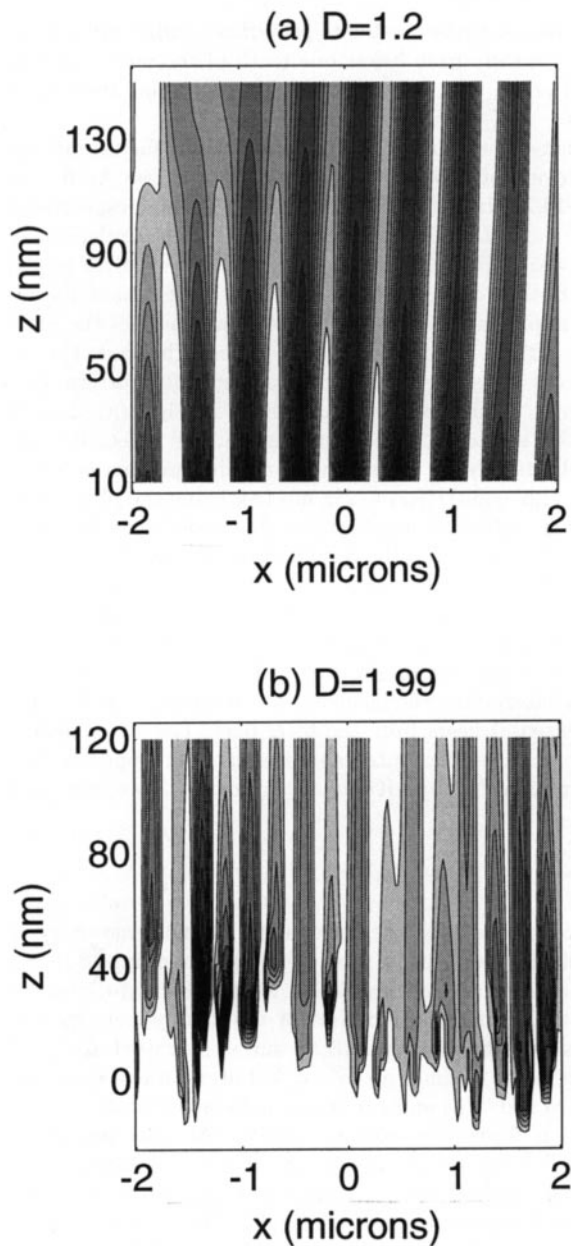


Fig. 4. Same as Fig. 3 but only for the doubly (and highly) scattered field intensity and a smaller near-field region. (a) $D = 1.2$ and $I_{\max} = 0.00056$; (b) $D = 1.99$ and $I_{\max} = 0.02$.

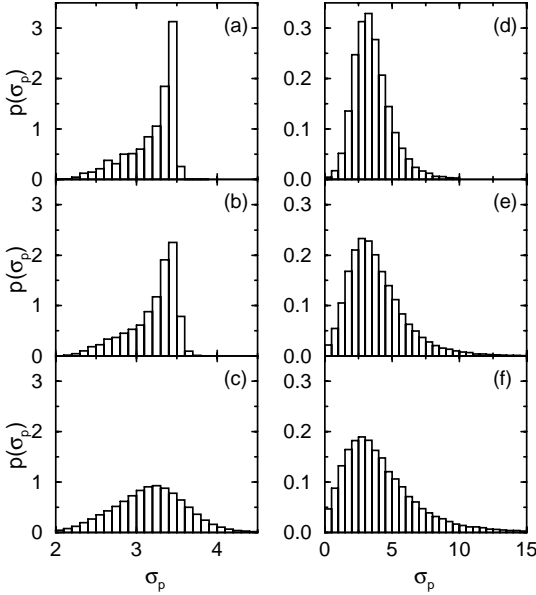


Fig. 5. PDF of the p -polarized FE factor $p(\sigma_p(\omega))$ for Ag fractal surfaces with rms height $\delta = 25.725$ nm and several fractal dimensions: $D = 1$ (a), 1.2 (b), 1.5 (c), 1.8 (d), 1.9 (e), and 1.99 (f). Other parameters are: $\lambda = 514.5$ nm ($\epsilon^< = -9.4 + i0.8$), $W/\lambda = 10 \cos \theta_0$, $L = 20.58$ nm, and $N = 800$. Average over $N_{data} = 200000$ points from $N_r = 20$ realizations and $\theta_0 = 0^\circ, 5^\circ, \dots, 60^\circ$.

$D = 1.2$ the intensity of this field component is very weak (two orders of magnitude smaller than the incident field), there exist very strong intensities in Fig. 4(b), comparable to those of the incident and singly scattered EM fields. Further evidence that the roughness-induced excitation of SPP is responsible for the occurrence of large FE is given by the polarization selectivity (the results for s polarization, not shown here, yield no relevant FE).

5 Surface EM Field Enhancement

Since the higher FE values are found precisely on top of the metal surface, in what follows we concentrate on the roughness and frequency dependence of the surface EM field. For the random surfaces we are dealing with, this surface EM field is a stochastic variable [24,26], so that its PDF will be studied below. To that end, the FE factor [cf. (10)] is calculated within the central region of the incident beam spot $-W/\cos \theta_0 < x < W/\cos \theta_0$ on every surface profile from a set of $N_r = 20$ realizations, and for several angles of incidence $\theta_0 = 0^\circ, 5^\circ, \dots, 60^\circ$. The PDF $p(\sigma_\beta(\omega))$ is then obtained from 200000 data points.

5.1 Surface Roughness: Fractality and RMS Height

Figure 5 shows the $p(\sigma_p(\omega))$ for Ag fractal surfaces with $\delta = 25.725$ nm and different local fractal dimensions $D = 1, 1.2, 1.5, 1.8, 1.9, 1.99$, at the wavelength $\lambda = 514.5$ nm ($\epsilon_{Ag}^<(\omega) = -9.4 + i0.8$). It is evident in Fig. 5 the

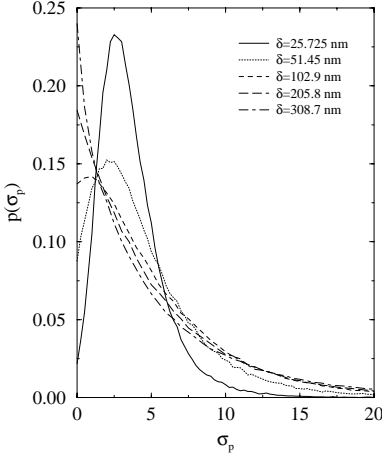


Fig. 6. Same as Fig.5(e), but for δ (nm)=25.725, 51.45, 102.9, 205.8, and 308.7.

strong dependence of the FE on the fractality of the rough surface. When the fractal dimension is small, the excitation of SPP is weak [see also Fig. 3(a) for $D=1.2$], and the surface EM field is basically given by the Kirchhoff approximation [cf. (11)]. This is clearly seen in Figs. 5(a) and (b) for $D = 1$ and 1.2 , respectively: $p(\sigma_p)$ takes the form of a convolution of narrow distributions for each θ_0 centered about the flat surface FE factor $\sigma_p^{(0)} \approx |1 + R_p(\theta_0)|^2$ (with the maximum close to the normal incidence value $\sigma_p^{(0)} \sim 3.53$). Upon increasing the fractal dimension, the roughness-induced excitation of SPP increases so that the surface FE can reach values larger than $\sigma_p^{(0)}$ (and also smaller, as expected from energy conservation). The distribution of $p(\sigma_p)$ thus widens as seen in Figs. 5(c) and (d) for $D = 1.5$ and 1.8 . For high fractal dimensions $D = 1.9$ and 1.99 , the larger surface FE values are encountered, and the broadening of the PDF becomes even more pronounced, manifesting a slow decay for values of σ_p beyond the maximum probability [see Fig. 5(e) and (f)]. Our results for Au and Cu, not shown here, manifest the same dependence of the PDF on the fractal dimension.

Therefore, despite the fact that the rms deviation of heights of the ensembles of random fractal surfaces used in Fig. 5 are all the same, the PDF differs significantly from one fractal surface to another, in such a way that the higher the local fractal dimension is, the larger are the surface FE found. The physical reason for this behavior has been pointed in [24]. The surface power spectrum, which plays the role of the scattering potential, exhibits a power law decay –with increasing spatial frequency– that is slower for higher D . Hence, upon increasing the fractality the roughness-induced photon-SPP coupling is favored, which lies on the basis of the existence of large FE for the configuration being considered.

In Fig. 6 the influence of the rms roughness is shown by plotting $p(\sigma_p)$ for δ (nm) = 25.725, 51.45, 102.9, 205.8, and 308.7, in the case of $D = 1.9$ [the

other parameters as in Fig. 5(e)]. Note that the increase of the rms height further broadens the PDF: In fact, the maximum probability shifts to lower values of σ_p (down to zero for $\delta > 102.9$ nm). Nevertheless, the tail of the distribution substantially grows, thereby revealing the occurrence of large surface FE. We have found values of up to $\sigma_p^{max} \gtrsim 10^3$, not only for the Ag fractal surfaces used in Fig. 6, but also for Au and Cu surfaces with analogous roughness parameters; the average surface FE's, however, lie well below (about 2 orders of magnitude). Interestingly, we have not gone further up in the increase of δ for the sake of computation constraints (namely, large number of points N required to accurately sample such fractals with steep slopes). With increasing roughness, the onset of the Anderson localization regime [27,28], owing to the strong SPP interference induced by the randomness, also helps to reinforce the surface FE. Anyhow, it should be mentioned that the SPP reradiation mechanism beyond some value of δ prevents σ_p from becoming arbitrarily large in this configuration [28]. This is what the results shown in Fig. 6 seem to indicate, for the tail growth saturates beyond $\delta = 102.9$ nm.

In light of the results of Fig. 6, it is tempting to say that large σ_p would also appear for the surfaces with small D by sufficiently raising δ . We have verified that this is not the case by calculating $p(\sigma_p)$ as in Fig. 5(b) with $D = 1.2$ but for $\delta = 514.5$ nm (not shown here). In spite of the strong rms height of this fractal surface (formally equivalent to a large overall scattering potential), the fact that the relative weight in the surface power spectrum of the higher spatial frequency components with respect to the lower ones is preserved (for it only depends on D) hinders the excitation by light of SPP (and thus the related FE) for $D < 1.5$. It is worthwhile mentioning, however, that a weak FE not connected to the SPP excitation can be observed within the selvedge of this kind of surfaces when the rms height is high enough as to ensure the occurrence of double (or higher) scattering processes in the geometrical optics sense; this has been addressed in [28]. This kind of weak FE, which we believe irrelevant to SERS in most widely used experimental configurations, is also found for s -polarized waves. In this regard, we would like to point out that $p(\sigma_s)$, although not shown here, resembles for all the fractal surface parameters considered thus far the narrow distribution of $p(\sigma_p)$ for $D = 1$ shown in Fig. 5(a), confirming that no significant FE takes place for s polarization (transverse electric modes).

5.2 Excitation Frequency: Ag, Au, Cu

The wavelength dependence of $p(\sigma_p(\omega))$ is studied in Fig. 7 for $D = 1.9$ and $\delta = 102.9$ nm for the excitation wavelengths $\lambda(\text{nm}) = 413.3, 514.5, 619.9, 729.3, 826.6$, and 1064 (where the experimental values of the Ag dielectric function at such wavelengths are obtained from [32]). When the wavelength diminishes, the maximum probability value decreases approximately following the Fresnel coefficient dependence at normal incidence [cf. (11)]. At the same

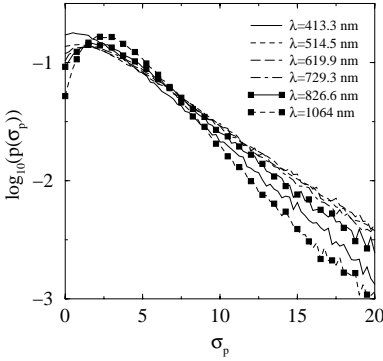


Fig. 7. PDF of the p -polarized FE factor $p(\sigma_p(\omega))$ in a log scale for Ag fractal surfaces with $D = 1.9$ and $\delta = 102.9$ nm: $\lambda(\text{nm}) = 413.3, 514.5, 619.9, 729.3, 826.6$, and 1064 (correspondingly, $\epsilon^< = -4.41 + i0.73, -9.4 + i0.8, -15.04 + i1.02, -22.45 + i1.4, -30.2 + i1.6$, and $-48.8 + i3.16$). Other parameters as in Fig. 5.

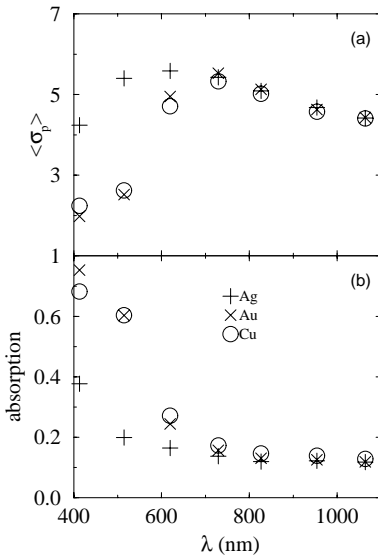


Fig. 8. Spectral dependence of (a) mean FE and (b) absorption for the same fractal surface used in Fig. 7. (+), Ag; (x), Au; (o), Cu.

time, the distribution widens for lower wavelengths, indicating that the fractal surface scatters light relatively more strongly. This stems from two facts: on the one hand, the Ag surface-plasmon wavelength $\lambda_{SP} = 2^{1/2}\lambda_p \approx 222.2$ nm is being approached [12]; on the other, the roughness parameters in terms of the excitation wavelength become larger for smaller wavelengths. With respect to the occurrence of large FE, we observe in Fig. 7 that the tail of large $\sigma_p(\omega)$ is built up with decreasing wavelength down to $\lambda = 619.9$ nm, as somehow expected according to the preceding argument, but becomes smaller again upon further lowering the excitation wavelength to $\lambda = 413.3$ nm.

This is more clearly seen in Fig. 8(a), which shows the wavelength dependence of the ensemble average value of σ_p for Ag, Au, and Cu. The experimental values of the dielectric functions for Au and Cu are also obtained from [32]. The behavior for the lower wavelengths is due to the increase of

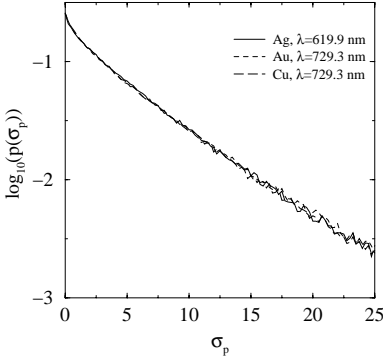


Fig. 9. PDF of the p -polarized FE factor $p(\sigma_p(\omega))$ in a log scale for Ag, Au, and Cu fractal surfaces with $D = 1.9$ and $\delta=308.7$ nm at the optimum excitation frequency. Solid curve: Ag at $\lambda = 619.9$ nm; dashed curve: Au at $\lambda = 729.3$ nm; long-dashed curve: Cu at $\lambda = 729.3$ nm. Correspondingly, $\epsilon_{Ag}^< = -15.04 + i1.02$, $\epsilon_{Au}^< = -18.9 + i1.43$, $\epsilon_{Cu}^< = -19.6 + i1.98$. Other parameters as in Fig. 5.

the bulk absorptive losses of propagating SPP when approaching the surface-plasmon wavelength. This increase in the absorption is strengthened for Au and Cu, since the onset of interband transitions for these two metals, which contribute to raise considerably the imaginary part of the dielectric function [32], is reached for the wavelength $\lambda \approx 500$ nm, in contrast to the case of Ag, for which this onset does not appear within the frequency range covered by Fig. 8. For large wavelengths, $\langle \sigma_p \rangle$ behaves similarly for the three metals, diminishing as the ratio of the roughness parameters to the incident wavelength also decreases (namely, the incident radiation tends to “see” a smoother surface). Therefore, Fig. 8 indicates that there exists an optimum excitation wavelength, about $\lambda = 619.9$ nm for Ag and $\lambda = 729.3$ nm for Au and Cu, at which the maximum σ_p is found for the kind of fractal surfaces dealt with in this work.

In Fig. 8(b) the absorption spectrum derived from the average reflectance calculations upon exploiting energy conservation, is shown for the fractal surfaces used in Fig. 8(a). Interestingly enough, in our case the maximum in the absorption spectrum does not necessarily correlate to the maximum FE, for there are no narrow resonances. As a matter of fact, it should be mentioned that the preceding argument is valid as long as no other frequency-selective mechanisms are present, such as localized surface plasmons associated with EM surface-shape resonances [6] or even electronic transition resonances [9].

Finally, we compare in Fig. 9 the $p(\sigma_p)$ for Ag, Au, and Cu, at the corresponding optimum excitation wavelengths [see Fig. 8(a)], in the case of a fractal surface characterized by $D = 1.9$ and $\delta = 308.7$ nm. The three curves lie practically on top of each other, revealing almost identical behavior for these metal surfaces provided that the optimum excitation frequency is used. Again, the latter statement is only true in the absence of narrow resonances. A resonance lying within the range of interband transitions for Au and Cu, but outside the range for Ag, would lead to a much lower FE for Au and Cu than for Ag, owing to damping. In general, the fact that the onset of such transitions in Ag occurs at a wavelength $\lambda \approx 300$ nm, favors its use as a SERS substrate.

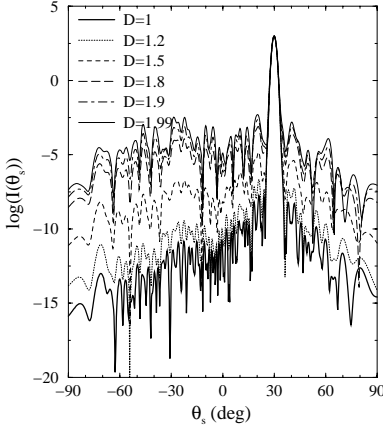


Fig. 10. Angular distribution of the speckle pattern intensity scattered from the fractal profiles shown in Fig. 2 for p polarization, $\lambda = 514.5$ nm, $\theta_0 = 30^\circ$, $W/\lambda = 10 \cos \theta_0$, $L/\lambda = 40$, and $N = 800$: $D = 1, 1.2, 1.5, 1.8, 1.9$, and 1.99 . The dielectric permittivity of silver is: $\epsilon = -9.4 + i0.8$.

6 Far Field

The angular distribution of far field scattered into the vacuum half-space above the interface is not typically studied in SERS calculations, since most experimental works measure the SERS signal either at a fixed scattering angle or by collecting all angles with a focusing lens. Nevertheless, the complete description of the far field is a classical problem by itself merely from the scattering theory, and might help to deepen our understanding in SERS. It can be calculated from (9) once the two source-like surface functions are obtained as mentioned in Sect. 2. Particularly, we study the angular distribution of mean scattered intensity (MSI) by means of Monte Carlo simulation calculations for different fractal dimensions.

The angular distribution of the speckle pattern intensities scattered from the fractal silver surfaces plotted in Fig. 2 is shown for p polarization in Fig. 10 for an angle of incidence $\theta_0 = 30^\circ$. Leaving aside the specular peak (which is not suppressed for the value of the surface rms height δ/λ considered in Fig. 10), there exist differences between the speckle patterns for different fractal dimensions. Away from the specular direction, upon increasing the fractal dimension, the speckle intensity for both polarizations builds up and its oscillations become broader and less pronounced, manifesting the gradual onset of the higher spatial frequencies relative to the lower ones.

To analyze the differences observed in the averaged properties of these speckle patterns, the angular distribution of the diffuse component of the MSI is shown in Fig. 11 for $\theta_0 = 0^\circ$ and 30° for p polarization. Despite that, of course, the specular component is absent in Fig. 11, it is seen therein that a diffuse peak appears at the specular direction in all cases. This specular peak is higher and narrower the smaller the fractal dimension D is. However, the total diffusely scattered energy (integrated over all scattering angles) keeps constant regardless of the value of D . On the other hand, it should be emphasized that the *p*-polarized component is more strongly scattered

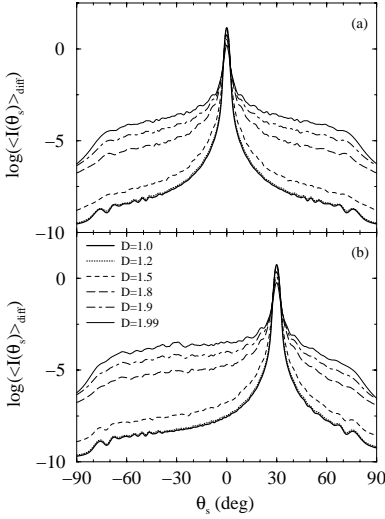


Fig. 11. Angular distribution of the diffuse component of the mean scattered intensity from silver, self-affine fractal surfaces for p polarization, $\lambda = 514.5$ nm, $\delta/\lambda = 0.05$, $W/\lambda = 10 \cos \theta_0$, $L/\lambda = 40$, and $N = 800$. Average over $N_r = 400$ realizations. Several fractal dimensions are considered: $D = 1, 1.2, 1.5, 1.8, 1.9$, and 1.99 . (a) $\theta_0 = 0^\circ$, (b) $\theta_0 = 30^\circ$. The dielectric permittivity of silver is: $\epsilon = -9.4 + i0.8$.

and gives rise to a broader angular distribution of MSI than the s -polarized component (not shown here, cf. [25]).

The results of Fig. 11 can be qualitatively interpreted in light of the power spectrum of the fractal surfaces $g(|k|)$ (k being the spatial frequency), which accounts for the contribution to the diffuse MSI to lowest (second) order in the surface height through $g((\omega/c)|\sin \theta_s - \sin \theta_i|)$. In the case of the self-affine fractal surfaces we are considering here, the power spectrum is a power law with a negative exponent whose absolute value decreases with increasing fractal dimension [31]. This indicates that the larger the fractal dimension D is, the broader the angular distribution of $\langle I^\gamma(\theta_s) \rangle_{diff}$ should be, as the curves in Fig. 11 reveal. The success of this simple argument suggests that a small-amplitude perturbation theory of the diffusely scattered intensity would suffice to describe, even quantitatively, the results shown in Fig. 11, considering how small the parameter δ/λ is. This might be the case for the lower fractal dimensions $D \leq 1.5$. Nonetheless, it does not apply to the surfaces with higher fractal dimensions.

The presence of higher spectral components in the surfaces with larger fractal dimensions should enhance the excitation of surface-plasmon polaritons in p polarization, as inferred from the behavior of the surface magnetic field and the occurrence of large field enhancements (see Sect. 4 above). This would lead to the appearance of enhanced backscattering in the diffusely scattered intensity, resulting from multiple scattering interference mediated by the excited surface-plasmon polaritons. As expected, the results for p polarization and $\theta_0 = 20^\circ$ shown in Fig. 12 for a fractal profile of $D = 1.95$ and $\delta/\lambda = 0.2$ exhibit a weak backscattering peak; this peak is absent from the result for s polarization.

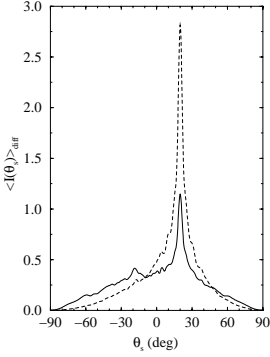


Fig. 12. Same as Fig. 11(a) but for $D = 1.95$, $\theta_0 = 20^\circ$, $\delta/\lambda = 0.2$, and $N_r = 500$. Solid curve: p polarization; Dashed curve: s polarization.

7 Concluding Remarks

We have seen that the rigorous scattering theory formulation based on the exact Green's theorem integral equations can be successfully applied to account in the full electrodynamic sense for the near EM field found on a corrugated metal surface illuminated by an incoming monochromatic beam. The occurrence of large FE in the vicinity of self-affine fractal surfaces of Ag, Au, and Cu has been explored through numerical simulation calculations of both the near field pattern and the PDF of surface field enhancements $p(\sigma_\beta)$. This is important to the understanding of the SERS EM mechanism on substrates consisting of fractally corrugated metal surfaces.

The near field intensity contour maps give a rigorous picture of the EM scattering mechanisms in the vicinity of the vacuum/metal interface. The behavior of the non-specular component of the scattered field intensity as a function of the spatial coordinates indicates for p polarization the existence of forward and backward propagating SPP along the interface whose amplitude decays exponentially away from the mean surface profile. This in turn reveals that the roughness-induced excitation of propagating, p -polarized SPP lies on the basis of the occurrence of large FE relevant to SERS in this configuration. The calculated PDF of the surface FE accounts for the transition from a narrow distribution centered about the planar surface FE [cf. (11)] for weakly scattering surfaces, to a broad, slowly decaying function when large σ_p takes place. In addition, the $\sigma_p(\omega)$ for a given frequency increases with the local fractal dimension and with the rms height. Fractality seems to be more critical: no significant surface FE are encountered for small local fractal dimensions regardless of the rms height, whereas for large D even a very low surface roughness $\delta/\lambda \sim 0.05$ suffices to produce moderate FE.

The frequency dependence analysis of the PDF of surface FE manifests the existence of an excitation wavelength for which the surface FE is maximized. This optimum excitation wavelength observed for large fractal dimensions (at about $\lambda \approx 620$ nm for Ag, $\lambda \approx 730$ nm for Au and Cu) stems from a compromise between the fractal scatterer strength (given by the roughness

parameters normalized by the incident wavelength) responsible for light-SPP coupling, and the SPP absorptive losses within the bulk metal. In addition, it has been shown that the optimum wavelength does not coincide with that at which the absorption spectrum yields a maximum. (Recall also that no frequency resonances are present here.) All Ag, Au and Cu surfaces manifest similar abilities to produce large FE's provided that the corresponding optimum excitation wavelength is used.

Large local FE maxima have been found ($\sigma_p \leq 10^3$, so that $\sigma^{SERS} \approx 10^6$); however the average values are relatively modest. Leaving aside the existence of other non purely EM mechanisms, we believe this to be due to the choice of fractal surface model, which nonetheless has proven to be very useful for both understanding the EM processes being involved and quantitatively establishing rigorous criteria as to the role played by surface fractality. The EM scattering formulation presented here could be used to study other surface models and even adapted to take into account more complicated configurations.

On the other hand, the angular distribution of the diffuse component of mean scattering intensity exhibit a specular peak: The larger is the fractal dimension, the broader and smaller this peak becomes. This is qualitatively explained in terms of the power spectrum of the surface roughness (which partially accounts in turn for the lowest order contribution in the surface height to the perturbative expansion of the MSI), given by inverse power laws with a slower decay rate for the self-affine fractals with higher fractal dimensions. In addition, a small backscattering peak in p polarization is found for fractal surfaces with large fractal dimension and sufficiently large rms height (but smaller than the wavelength), as a manifestation of the weak localization of surface-plasmon polaritons.

8 Perspectives

One of the limitations of the analysis of the surface FE shown in Sect. 5 is the fact that it is based on the magnetic field calculations. Although this is strongly recommended for such one-dimensional geometries and linear transversal-magnetic polarization from the theoretical and computational standpoints, it is nonetheless true that the physical quantity that the molecule *sees*, entering into the Raman polarization vector scaled by its Raman polarizability, is the electric field. Though the FE calculations based on the magnetic field are inherently related to those based on the electric field, information on polarization is surely lost. We have put forth a simple method to calculate the normal and tangential components of the electric field [33] that permits to address in detail the surface electric FE along preferred directions, relevant to SERS selectivity rules.

In addition, rigorous models describing the scattering of the Raman signal coming from the molecule and detected in the far field, and thus the

corresponding Raman FE, should follow the present work. Dipoles standing for single-molecule vibrating modes have been widely used in the literature, though typically nearby simplistic metal surfaces. This has to be done for realistic metal surfaces as the those dealt with here. Other approach we are working on consists of a surface Raman polarization discontinuity [34] that could be applied to Langmuir-Blodgett films [9].

In spite that SERS spectroscopy is a well established technique, the aforementioned theoretical works might shed light into it, particularly bearing in mind the recent experimental work reporting on SERS single-molecule detection through near-field optical microscopy and claiming the existence of anomalously large SERS FE factors [35]. Furthermore, new interesting phenomena and/or experimental configurations can be predicted from such studies.

9 Acknowledgement

This work was supported by the Spanish Dirección General de Investigación Científica y Técnica, through Grant No. PB97-1221, and Consejo Superior de Investigaciones Científicas. Partial support from a CSIC-CONACYT mobility Grant is also acknowledged.

References

1. M. Fleischmann, P. J. Hendra, and A. J. McQuillan (1974) *Chem. Phys. Lett.* **26**, 123
2. D. L. Jeanmaire and R. P. VanDuyne (1977) *J. Electroanal. Chem.* **84**, 1
3. M. G. Albrecht and J. A. Creighton (1977) *J. Am. Chem. Soc.* **99**, 5215
4. A. Otto (1984) in *Light Scattering in Solids IV*, edited by M. Cardona and G. Güntherodt (Springer-Verlag, Berlin), p. 289.
5. M. Moskovits (1985) *Rev. Mod. Phys.* **57**, 783
6. A. Wokaun (1985) *Molecular Phys.* **53**, 1
7. A. Otto (1991) *J. Raman Spectrosc.* **22**, 743
8. A. Otto, I. Mrozek (1992) H. Grabhorn, and W. Akemann, *J. Phys. Condens. Matter* **4**, 1143
9. R. Aroca and G. Kovacs (1991) in *Vibrational Spectra and Structure*, edited by J. R. Durig (Elsevier, Amsterdam), Vol. 19, p. 55.
10. A. Otto (1980) *Surf. Sci.* **57**, 309
11. V. M. Shalaev (1996) *Phys. Rep.* **272**, 61
12. H. Raether (1988) *Surface Polaritons on Smooth and Rough Surfaces and on Gratings* (Springer-Verlag, Berlin).
13. S. Sánchez-Cortés, J. V. García-Ramos, and G. Morcillo (1994) *J. Colloid Interface Sci.* **167**, 428 ; S. Sánchez-Cortés, J. V. García-Ramos, G. Morcillo, and A. Tinti (1995) *J. Colloid Interface Sci.* **175**, 358
14. D. P. Tsai, J. Kovacs, Z. Wang, M. Moskovits, V. M. Shalaev, J. S. Suh, and R. Botet (1994) *Phys. Rev. Lett.* **72**, 4149

15. M. C. Chen, S. P. Tsai, M. R. Chen, S. Y. Ou, W.-H. Li, and K. C. Lee (1995) Phys. Rev. B **51**, 4507
16. J. V. García-Ramos and S. Sánchez-Cortés (1997) J. Mol. Struct. **405**, 13
17. C. Douketis, Z. Wang, T. L. Haslett, and M. Moskovits (1995) Phys. Rev. B **51**, 11022
18. R. Jullien and R. Botet (1987) *Aggregation and Fractal Aggregates* (World Scientific, Singapore)
19. A.-L. Barabási and H. E. Stanley (1995) *Fractal Concepts in Surface Growth* (University Press, Cambridge)
20. M. Xu and M. J. Dignam, J. Chem. Phys. **96**, 7758 (1992); **99**, 2307 (1993); **100**, 197 (1994)
21. E. Y. Poliakov, V. M. Shalaev, V. A. Markel, and R. Botet (1996) Opt. Lett. **21**, 1628
22. F. Brouers, S. Blacher, A. N. Lagarkov, A. K. Sarychev, P. Gadenne, and V. M. Shalaev (1997) Phys. Rev. B **55**, 13 234
23. F. J. Vidal and J. B. Pendry (1996) Phys. Rev. Lett. **77**, 1163
24. J. A. Sánchez-Gil and J. V. García-Ramos (1997) Opt. Commun. **134**, 11
25. J. A. Sánchez-Gil and J. V. García-Ramos (1997) Waves in Random Media **7**, 285
26. J. A. Sánchez-Gil and J. V. García-Ramos (1998) J. Chem. Phys. **108**, 317
27. A. A. Maradudin, T. Michel, A. R. McGurn, and E. R. Méndez (1990) Ann. Phys. NY **203**, 255
28. J. A. Sánchez-Gil and M. Nieto-Vesperinas (1991) J. Opt. Soc. Am. A **8**, 1270 ; (1992) Phys. Rev. B **45**, 8623
29. M. Nieto-Vesperinas (1991) *Scattering and Diffraction in Physical Optics* (Wiley, New York)
30. M. Nieto-Vesperinas and J. A. Sánchez-Gil (1992) J. Opt. Soc. Am. A **9**, 424
31. R. F. Voss (1989) in: *The Science of Fractal Images*, edited by H.-O. Peitgen and D. Saupe (Springer, Berlin, 1988); R. F. Voss, Physica D **38**, 362
32. D. W. Lynch and W. R. Hunter (1985) in: *Handbook of Optical Constants of Solids*, edited by E. D. Palik (Academic Press, New York), p. 356.
33. J. A. Sánchez-Gil, J. V. García-Ramos, and E. R. Méndez, to be published.
34. E. R. Méndez, J. A. Sánchez-Gil, and J. V. García-Ramos, to be published.
35. S. Nie and S. R. Emory (1997) Science **275**, 1102